# On the Structure-Properties Relationship in Montmorillonite-Filled Polyamide 6 Nanocomposites

**Mladen Motovilin, Zlatan Denchev, Nadya Dencheva**

I3N—Institute for Polymers and Composites, University of Minho, campus Azurém, Guimarães 4800-058, Portugal

**ABSTRACT:**

Polyamide 6/montmorillonite (MMT) nanocomposites were prepared by melt compounding method comprising 1–7.5 wt % of Nanomer I.24 TL or 5 and 10 wt % of Cloisite 15A organically modified nanoclays. The composite samples were characterized by synchrotron X-ray, thermal and FT-IR spectroscopy methods looking for changes in the micro- and nanostructure of both PA6 matrix and MMT reinforcement as a function of the clay content and type. These data were discussed in conjunction with the mechanical properties of the respective nanocomposites. Generally, the Young's modulus was found to increase proportionally to the clay content being the highest in samples with strong aggregation of MMT at micron length scale.

The tensile strength passed through a maximum at 2.5 wt % clay load presenting a homogeneous microstructure with almost no agglomeration. Increasing the amount of MMT produced less crystalline PA6 matrices, richer in gamma-PA6 polymorph and resulted in larger long spacings of PA6 due to expansion of both crystalline and amorphous domains.

*Wiley Periodicals, Inc. J Appl Polym Sci 120: 3304–3315, 2011*

**Key words:** nanocomposites; polyamides; structure-property relation; X-ray scattering; FT-IR

## INTRODUCTION

Nanostructured polymer composites comprising layered silicate clays have been intensively studied in recent years. These materials comprise a polymer matrix reinforced by well-dispersed clay platelets with at least one dimension in the nanometer range.[1] Addition of minimal concentrations of nanosized clay (typically less than 10 wt %) can enhance significantly important properties of the matrix polymer, e.g., mechanical strength and stiffness [2–4] thermal stability and heat distortion temperature,[5–8] flame retard-ancy,[9,10] gas barrier performance.[11,12] Among the great variety of naturally available layered silicate minerals, montmorillonite (MMT) is particularly attractive as reinforcement of polymers because it is environ-mentally friendly and readily available in large quantities at relatively low cost. Moreover, MMT platelets possess high aspect ratio with layer thicknesses of ca. 1 nm and lateral dimensions ranging from 30 nm to several microns.[13] For better compatibility with the polymer matrix, the platelets' surface can be converted from hydrophobic to organophilic via cation exchange of the Na+ of pristine MMT with alkylammonium ions including primary, secondary, tertiary, and quaternary alkylammonium cations under proper conditions.[14]

In general, thermoplastic polymer nanocomposites are prepared by three methods: (i) in situ intercalative polymerization of monomers, (ii) polymer intercalation by the solution method, and (iii) melt blending.[15] The third method has the advantage of being entirely compatible with the industrial polymer processing techniques without any use of organic solvents, expensive reagents, or polyamides.[6]

Nanocomposites based on polyamide 6 (PA6)/MMT are among the best studied and have therefore gained major industrial importance. The melt blending of organophilic MMT (o-MMT) and PA6 is performed typically in extruders.[17–19] In the early 1990s Toyota Group developed and was probably the first to realize industrially the preparation of PA6 nanocomposites via in situ intercalative polymerization. [7,20,21] Since then, numerous articles have been published on PA6/MMT nanocomposites obtained by either melt blending or in situ polymerization. It has been recognized that understanding the synthesis-structure-properties relationship is vital for the development of nanocomposites with enhanced mechanical properties.

X-ray diffraction has been used in almost every published study to monitor the type of distribution of the clay platelets (intercalated or exfoliated). Less frequently the crystallinity index of the PA6 matrix and the content of the two PA6 polymorphs (a and c crystalline forms) have been studied in commercial X-ray machines as a function of the MMT type and content.[22,23] For more sophisticated structural studies wide- and small-angle X-ray scattering (WAXS, SAXS) from synchrotron has been used.[24-27] The matrix polymorphic structure and its crystalli-zation/melting behavior can also be studied by differential scanning calorimetry.[3,28,29] The thermogravimetric analysis (TGA) helps determine the exact amount of MMT in the nanocomposites and characterize the rate of their thermodegradation.[30,31] Spectroscopic techniques such as FT-IR can register the polymorph content of the matrix PA6 and structural changes in MMT after its treatment, including the presence of organic surfactants.[17,32]

All of the aforementioned structural parameters can have an influence on the mechanical properties of the PA6/MMT nanocomposites. Unfortunately, direct comparison of structural data obtained by different researchers does not seem to be straightforward because of the variations in the MMT type and organic pretreatment, different polyamide grades, incomparable preparation and testing conditions of the nanocomposites samples. In the present article we report on the structure-mechanical properties relationship in nanocomposite samples prepared in controlled conditions, based on the same PA6 grade and two commercial MMT brands. Data from synchrotron WAXS and SAXS, DSC, TGA and FT-IR microscopy were discussed in conjunction with the mechanical properties of the respective nanocomposites sample. The paper is a part of a comprehensive study on the synthesis and properties of hybrid composites comprising a polyethylene isotropic matrix reinforced by polyamide microfibrils that contain MMT with various concentrations and degrees of exfoliation.

## EXPERIMENTAL

### Raw materials

The neat hydrolytic PA6 (trade name Durethan B30S, pellets) used in this work was obtained from Lanxess (Leverkusen, Germany). The pelletized masterbatch of PA6 with predispersed/exfoliated organophilic MMT (trade name Nanomer I.24 TL) called ''nano-PA6 concentrate'' (NPC) with a clay content of 17–20 wt % is a product of Nanocore (Arlington Heights, IL). According to the information provided by the manufacturer, this clay has 12-aminododecanoic acid as surfactant, the typical aspect ratio of the monolayers is 200–400, the maximum moisture content is 12% and the cation exchange capacity (CEC) is 145 meq/100 g. The other clay used in this study is Cloisite 15A delivered by Southern Clay Products (Gonzales, TX) representing natural MMT modified with dimethyl dihydrogenated tallow quaternary ammonium chloride with a CEC of 115–125 meq/100 g, moisture content of 14% and organic content of 43% (manufacturer's data). The aspect ratio of the monolayers in this brand is 75–100.[33] All raw materials were dried for 12 h at 80ºC under slight vacuum before further use.

### PA6/MMT compounding and test sample preparation

The NPC masterbatch denoted as MB20NM was diluted (let down) with the respective amounts of neat PA6 to systems containing 1.0, 2.5, 5.0, and 7.5 wt % of MMT by melt blending in a Leistritz (Leistritz Produktionstechnik GmbH, Nuerenberg, Germany) counter-rotating twin-screw laboratory extruder with a medium to high shear configuration. The extruder operated at 100 rpm and a feed rate of 1.5 kg/h, adjusted gravimetrically. The temperature was set to 245ºC for all seven heating zones. A two-hole die with 2 mm diameter for each hole was used. The extruder line integrated also a cooling bath and a cutting device equipped with air drier. The same extruder line configuration and conditions were used to obtain a dispersion of 10 wt % Cloisite 15A (MB10CL) consequently let down to 5 wt % with neat PA6. The pelletized PA6/MMT nanocomposites containing different amounts of Nanomer or Cloisite clays were dried for 12 h and compression-molded into plates with a thickness of 1.0± 0.1mm in a hot press with a pressure of about 10 tons/cm2 at 250ºC. Plates from the neat PA6, the MB20N and MB10CL compositions were also produced under the same conditions.

### Sample analyses

Tensile tests were performed in an Instron model 4505 testing machine (Instron, High Wycomb, UK). The tests were carried out at 23 6 2_C with a standard load cell of 1 kN at constant crosshead speed of 50 mm/min. Test samples had a gauge length and width of 25 mm and 4 mm, respectively. Ten specimens of each sample were studied to calculate the average and the standard deviation values. The nominal stress was determined as a ratio of the tensile force and the initial cross section of the sample. The nominal strain was determined as a ratio of the sample gauge length at any time during drawing and that prior to drawing. The Young's modulus values were calculated from the respective stress-strain curves at 1% strain (secant modulus).

The DSC measurements were made in a Diamond Pyris calorimeter of Perkin–Elmer (Waltham, MA) at a heating rate of 10ºC/min under $N_2$ purge. The typical sample weights were in the 13–15 mg range. The TGA analyses were carried out in TA Q500 gravimetric balance heating the samples to 600ºC at 10ºC/min in N2 or air atmosphere.

The FT-IR microscopy studies were performed in a Spotlight 300 IR microscope with a dual mode array detector allowing for singe-point spectra and IR imaging in the 4000–750 cm$^{-1}$ range with a resolution of 6.0 μm. For this analysis, slices with a thickness of 12 μm were produced from each sample in a Leitz 1401 microtome (Wetzlar, Germany) using a glass blade.

All WAXS and SAXS patterns in this study were registered at the Soft Condensed Matter Beamline (A2) of HASYLAB, Hamburg, Germany using synchrotron radiation with a wavelength fixed to 0.15 nm. The sample-to-detector distance for SAXS was set at 2830 mm, the diffraction patterns being registered by means of a MAR (Rayonix, Evanston, IL) two-dimensional (2D) detector. For the WAXS measurements the detector was positioned at 90 mm in respect to the sample. The samples were studied in transmission mode, the exposure time being 10 s for WAXS and 30 s for the SAXS patterns. A specially designed sample holder was used allowing for controlled heating-cooling cycles in the 30–300ºC. An Imago multichannel processor and program controller of Jumo GmbH and Co

KG (Fulda, Germany) were used to regulate the sample temperature in heating and cooling. The difference between the read-out and real temperature was found to be 3-4ºC at the heating rate of 20_C applied in this study.

To process the 2D WAXS and SAXS images, a commercial software package was used.[34] Corrections for background scattering, irradiated volume and beam intensity were performed for each image. The 2D SAXS patterns were integrated in the range of s values between 0 and 0.15 nm$^{-1}$. s is the scattering vector, whose modulus is defined as $|s| = (s_{1,2}^2 + s_3^2)^{0.5} = (2/\lambda)\sin\theta$. For the WAXS measurements the range was between scattering angles $2\theta$ of 2 and 40º

## RESULTS AND DISCUSSION

### Tensile properties

Figure 1 and Table I show the tensile behavior of the PA6 nanocomposites as a function of the o-MMT amount and type comparing it to the matrix PA6.
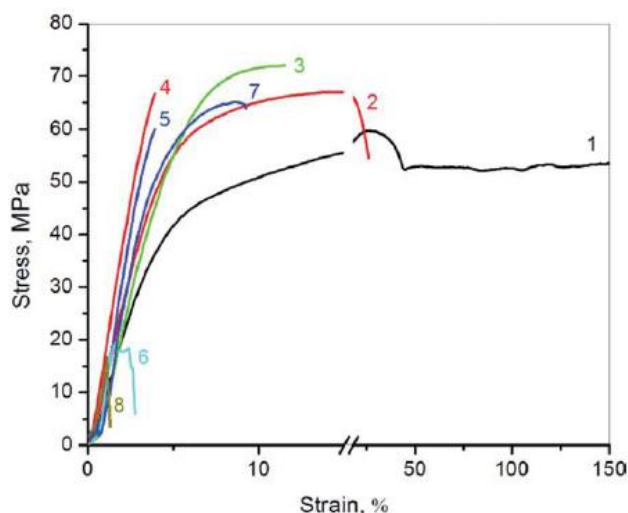


**Figure 1** Stress-Strain Curves of PA6/MMT Nanocomposites with various amounts and types of clay load: 1, neat PA6; 2, 1.0% Nanomer; 3, 2.5% Nanomer; 4, 5% Nanomer; 5, 7.5% Nanomer; 6, 20% Nanomer (MB20*N*); 7, 5% Cloisite 15A; 8, 10% Cloisite 15A (MB10CL). [Color figure can be viewed in the online issue, which is available at wileyonlinelibrary.com.]

Thus, the neat PA6 (curve 1) shows clear yielding and necking. This sample fails at a strain at break, $\varepsilon_{br}$, of ~160% and ultimate tensile stress $\sigma_y$ of 59 MPa, showing a Young modulus E of 1350 MPa. The stress-strain curves of the nanocomposites with 1.0–7.5% of MMT (Curves 2–5 and 7) have the typical brittle shape—without necking, the $\varepsilon_{br}$, values not exceeding 15% and the highest $\sigma_y$ values being between 67 and 72 MPa obtained with 1.0 and 2.5% NM samples. High loads of MMT as in the two masterbatches MB20NM and MB10CL (Curves 6 and 8) result in significant growth of the modulus values as compared with the matrix PA6 (ΔE ¼ 113 and 66%, respectively), but lead to a catastrophic decrease of the ry values (Table I). It can be

concluded that the nanocomposites with 2.5 and 5.0% Nanomer seem to show the best set of tensile properties: an improvement in respect to the matrix of 22 and 15% for $\sigma_y$ and 27 and 62% for the Young modulus. The latter can be enhanced further with higher loads of clay but in detriment of the ultimate tensile stress. These trends are similar with the Cloisite A nanoclay, the respective results for ΔE and Δ$\sigma_y$ always slightly lower as evident if comparing the 5% NM and 5%CL samples (Fig. 1, Curves 4 and 7; Table I). Such a mechanical behavior has been verified in many earlier studies on PA6-clay nanocomposites. In this work an attempt will be made to relate the tensile properties of the NM and CL-containing PA6 to the micro- and nanostructure of the composite materials.

### Thermogravimetric studies

Figure 2 shows a sample TGA curve whose inflection point that corresponds to the temperature of maximum degradation rate $T_{deg}$ was found by the peak of the first derivative. Table II shows the dependence of $T_{deg}$ and the percentage of the carbonized residue determined at 600ºC for all samples on the MMT type and content as determined in nitrogen and air atmospheres. The $T_{deg}$ can be related to the heat-resistance of the sample and the carbonized residue—with the real amount of MMT introduced into the composite. It can be seen that the residue at 600ºC in both atmospheres roughly corresponds to the amount of the MMT introduced into the PA6, whereby the higher the MMT load, the bigger the difference. A possible explanation of this observation is that the MMT in both NM and CL clays are organically treated and contain relatively volatile reagents (organic amines and fats) tending to evaporate more easily and causing a bigger weight loss of the residue at larger clay charges. As regards the $T_{deg}$, for the neat PA6 matrix, it is with 22ºC higher in nonoxidizing than in oxidizing atmosphere. Adding either NM or CL basically increases the $T_{deg}$ in air and decreases it in nitrogen. Therefore, the addition of MMT can improve the heat-resistance of the PA6 nanocomposites only in air.

### DSC studies

Figure 3 and Table III summarize the results of the DSC studies of all PA6/MMT samples. It can be seen that with MMT charges of 5.0 wt % and more the PA6 melting peak originally appearing at 220–222ºC splits into two peaks: one around 220ºC and another—in the range of 205-210ºC. On the basis of previous data on the polymorphism in PA6,[37] the latter was attributed to the melting of the more ductile γ-PA6 phase and the former—to the stiffer α-phase. Increasing the MMT charge results in a growth of the lower-melting c-phase and in a general drop of the DSC crystallinity index calculated from the relation of the total melting enthalpy DHm and the extrapolated enthalpy of a 100% crystalline PA6 (230 J/g). The glass-transitions Tg of all samples vary in the 46-48ºC range, the height of the step becoming lower as the filler amount increased.

TABLE I
**Mechanical Properties of PA6/MMT Nanocomposites Extracted from the Stress-Strain Curves**

| Sample | Young's modulus, $E$, MPa | $\Delta E$, % | Tensile strength $\sigma_1$, MPa | $\Delta\sigma_1$, % | Elongation at break, $\varepsilon$, % |
|---|---|---|---|---|---|
| PA6 | 1350 ± 17 | 0.0 | 59.3 ± 1.3 | 0.0 | 162.0 |
| 1% NM | 1640 ± 23 | 21.5 | 66.8 ± 2.2 | 12.6 | 15.0 |
| 2.5% NM | 1710 ± 41 | 26.7 | 72.1 ± 2.8 | 21.63 | 14.4 |
| 5% NM | 2180 ± 19 | 61.5 | 68.1 ± 3.1 | 14.9 | 4.0 |
| 7.5% NM | 2300 ± 22 | 70.4 | 59.9 ± 2.8 | 1.0 | 1.1 |
| 5% CL | 2001 ± 62 | 48.2 | 64.9 ± 2.8 | 9.6 | 9.7 |
| MB20NM | 2870 ± 43 | 112.6 | 18.9 ± 1.0 | −68.1 | 0.2 |
| MB10CL | 2230 ± 57 | 65.2 | 16.7 ± 1.0 | −71.8 | 1.1 |

CL, Cloisite 15A MMT clay; NM, Nanomer MMT clay originating from NPC concentrate.

**TABLE II**
**Data Obtained from the TGA of PA6/MMT Nanocomposites in $N_2$ and Air Atmospheres**

| Sample | Carbonized residue in $N_2$ , % | Carbonized residue in air , % | Peak $T_{deg}$ in $N_2$, °C | Peak $T_{deg}$ in air, °C |
|---|---|---|---|---|
| PA6 | 0.543 | 0.566 | 459.8 | 437.8 |
| 1 % NM | 1.575 | 1.828 | 456.2 | 444.4 |
| 2.5% NM | 2.777 | 2.773 | 452.7 | 444.5 |
| 5% NM | 4.852 | 4.882 | 450.5 | 456.7 |
| 7.5% NM | 6.934 | 7.055 | 450.0 | 450.4 |
| 5% CL | 4.779 | 4.563 | 452.5 | 458.0 |
| MB20NM | 17.890 | 17.133 | 440.0 | 448.2 |
| MB10CL | 9.720 | 8.511 | 440.0 | 450.2 |

CL, Cloisite 15A MMT clay; NM, Nanomer MMT clay originating from NPC concentrate. The temperature of the maximum degradation rate $T_{deg}$ is determined as the peak of the derivatized TGA curve (Fig. 2).
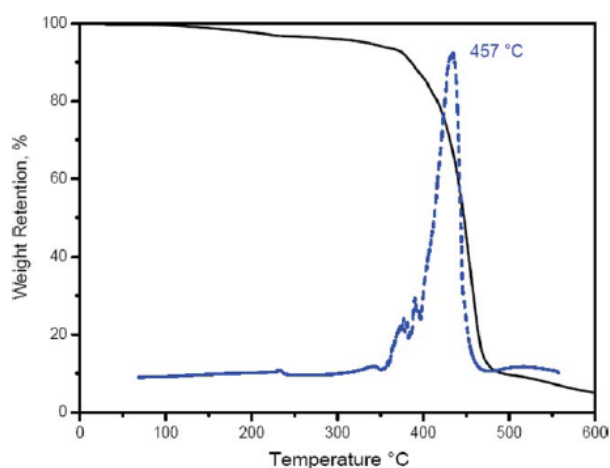


Figure 2 Representative TGA curve of the 5% NM nanocomposites (solid line); dashed line: derivatized TGA curve. For sample designation see Table I. [Color figure can be viewed in the online issue, which is available at wileyonlinelibrary.com.]



Figure 3 Selected DSC curves of: 1, neat PA6; 2, PA6/ MMT Nanomer 2.5 wt %; 3, PA6 MMT Nanomer 5.0%; 4, PA6 MMT Cloisite 5.0%; 5, MB20NM $T_m^1$ = melting temperature of the $\gamma$ -PA6; $T_m^2$ = melting temperature of the $\alpha$ -PA6. [Color figure can be viewed in the online issue, which is available at wileyonlinelibrary.com.]

The DSC data did not allow quantification of the polymorph content of the PA6 matrix, which was made on the bases of the WAXS curves of the samples.

**Structural studies by WAXS**

Most of the WAXS studies on polymer nanocomposites are confined to the change of the angular position of the (001) basal reflection of the layered clay mineral, related to the height of the galleries between the inorganic sheets.[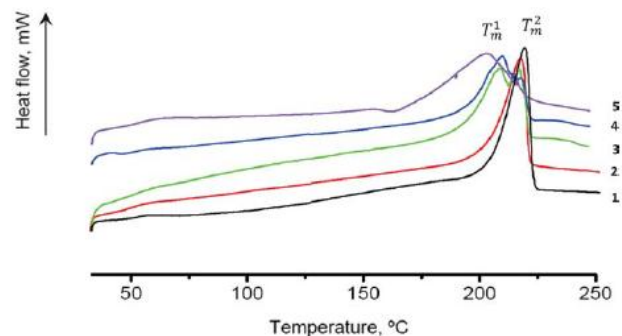22,23] The natural MMT comprises negatively charged silicate sheets with hydrated Na+ or Ca+ ions in the galleries. To get o-MMT, these small cations are exchanged with bulky organic amine cations resulting in a increase of the d(001) spacing, which corresponds to an expansion of the galleries height. At the same time, the nature of their surface changes from hydrophilic to organophilic allowing for a better compatibility with the matrix polymer. The latter is introduced into the galleries by either in situ polymerization or some processing technique including melt-mixing.[35]

| Sample | $T_m^1$ °C | $T_m^2$ °C | $X_c$ % |
|---|---|---|---|
| PA6 neat | – | 221.6 | 34.2 |
| 1 % NM | – | 223.5 | 35.4 |
| 2.5% NM | – | 219.7 | 29.3 |
| 5% NM | 210.7 | 219.8 | 26.4 |
| 7.5% NM | 205.4 | 218.4 | 20.2 |
| 5% CL | 210.0 | 219.7 | 26.0 |
| MB10CL | 211.0 | 220.8 | 20.0 |
| MB20NM | 204.8 | – | 19.0 |

For sample designation see Table I. $X_c$ = DSC crystallinity index obtained with the enthalpy of fusion of a 100% crystalline PA6 $H_m^{100} = 230.0$ J/g.

The further increase of the d(001) observed in the presence of the matrix polymer can be related to the various degrees of clay delamination denoted as intercalation and exfoliation. In this work an attempt is made to reveal how mixing of different o-MMT brands would affect the nanostructure of both nanoclay and matrix considering all their WAXS reflections.

Figure 4 compares the WAXS patterns of the two o-MMT sources used in this work—Nanomer I.24 TL and Cloisite 15A at 30ºC. The peak designation is according to Koh.[36] It can be seen that there exist small but clear differences between these two materials. The d001 values of the organically treated Cloisite and Nanomer (the 001om reflections) correspond to expanded gallery heights of ca. 29 and 20 Å respectively.
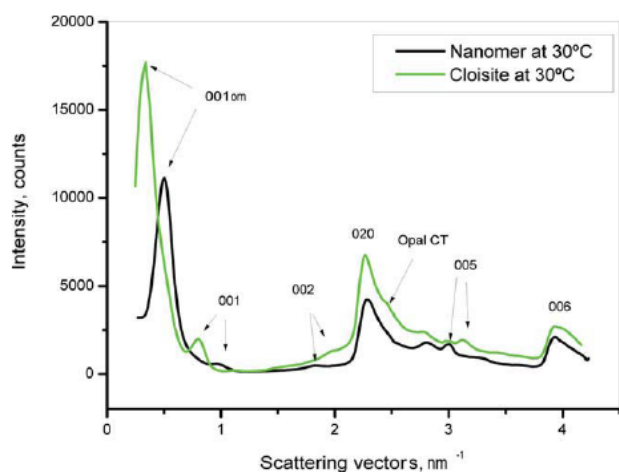


**Figure 4** WAXS patterns of the two montmorillonite brands of at 30°C. The peak indexation is according to Ref.[36] OM, organically modified. Opal CT, Opal cristobalite. [Color figure can be viewed in the online issue, which is available at wileyonlinelibrary.com.]

Some amounts of Na-MMT are also observable in both o-MMT samples (being larger in the Cloisite MMT), with 001 reflections corresponding to 12.4 and 10.0 Å. It is noteworthy that at 260ºC in the Nanomer MMT the intensities of both (001 om) and (001) reflections increased as compared with those in the same sample at 30ºC, while their angular positions remained unchanged. It was just the opposite in the Cloisite 15A sample — the intensities of the two reflections were higher at 30ºC than at 260ºC. In the latter case there was also a shift of the two peaks to higher values of the scattering vector, i.e., smaller long spacings. The above changes are reversible: when cooling down to 30ºC, in both o-MMT brands the intensities and the positions of the two peaks were restored. Most probably, the (001 om) and (001) reflections of the two o-MMT brands react differently to temperature changes since they are closely related to the type and degree of the clay organophylization which is different for Nanomer and Cloisite clays. Higher order MMT reflections were also identified in both samples in Figure 4. The strongest ones are those of the 020 and 006 crystalline planes, as well as of a specific crystalline phase called Opal Cristobalite (CT).[36,37] Their angular positions, shapes and intensities were found to be independent on the heat treatment temperature.

Figure 5 visualizes the way deconvolution and fitting of the WAXS patterns was performed for all PA6-MMT nanocomposites, exemplifying it for the PA6 hot-pressed plate containing 7.5% Nanomer at 30ºC. This treatment was performed to quantify the polymorphic transitions in PA6 and the changes in the MMT structure as its content was changed.
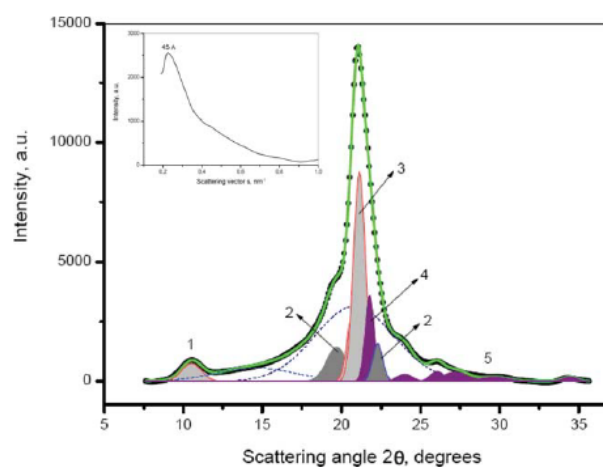


**Figure 5** Example of fitting the WAXS patterns of PA6 hot-pressed plate containing 7.5% NM: 1, 020 reflection of γ-PA6; 2, 200 and (002/202) reflection of the α-PA6; 3, 200 reflection of the γ-PA6; 4, Opal CT reflection of NM; 5, weaker reflections of the NM phase. The two broad Gaussian peaks represent the contribution of the diffuse scattering (amorphous halo). The inset shows the WAXS curve in the 0.1–1.0 nm$^{-1}$ range of the scattering vector **s**. For more details see the text. [Color figure can be viewed in the online issue, which is available at wileyonlinelibrary.com.]

The inset shows the range of the 001 reflection with its peak at s = 0.222 nm$^{-1}$ correspon-ding to a d-spacing of 45 Å. Decreasing the MMT amount, this value goes up to 48–50 Å, thus reaching the limit of resolution of the WAXS

setup used. This leads to the conclusion that the absence of a (001) basal peak of MMT may not necessarily mean complete exfoliation with distances between the silicate sheets of several nanometers and more. Nevertheless, in the presence of PA6 the galleries height of the o-MMT expands almost twice due to the effective intercalation of the polyamide macromolecules.

As suggested in previous works,[27,38,39] a monoclinic unit cell lattice was assumed for the a-PA6 form with two peaks corresponding to a(200) and a(002/202) crystalline planes with $2\theta$ being between 19 and 20º and 23 and 24º, respectively, (Fig. 5, the peaks denoted with 2). For the $\gamma$-crystalline form, pseudohexagonal unit cell was supposed, with one Gaussian for the c020 reflection (Peak 1) and two almost coinciding Gaussians for the c(001) and c(200) crystalline planes with $2\theta$ between 21 and 22º (Peak 3). From the MMT peaks in Figure 4, the Opal CT peak close to 22º was used in the fitting (Peak 4), as well as the series of weaker crystalline peaks in the angular range between 24º and 34º. Using these sets of MMT and PA6 peaks, excellent fits with $r^2 > 0.999$ were achieved. On their basis, the crystallinity indices, CI, and the relation between the two polymorphs was calculated for all nanocomposites samples as a function of the MMT type and concentration (Table IV). Apparently, with the increase of the Nanomer amount, the CI of the matrix gradually decreases. Moreover, the samples with 2.5 and 5.0% of Nanomer were richer in $\alpha$-PA6 polymorph while the sample with 7.5% NM and the NM masterbatch displayed significantly larger amounts of the $\gamma$-PA6. Comparing the nanocomposites with 5% of NM and 5% of CL shows that the latter nanoclay enhances stronger the formation of the $\gamma$-PA6 polymorph in the matrix. The same trend is revealed also in the two masterbatches MB20NM and MB10CL.

Figure 6 shows the temperature dependence of the WAXS patterns of 5NM and 5CL samples taken at 30, 160, 200ºC and at 30ºC after melting at 260ºC and subsequent recrystallization. Evidently, the Nanomer-containing sample [Fig. 6(a)] displays a clear $\alpha$ to $\gamma$-form transition at 160ºC but without revealing the $\gamma$(020) reflection (Curve 2). At 200ºC the $\alpha$-phase increases, too, as evidenced by the appearance of a shoulder at 23º (Curve 3). Melting at 260ºC and recrystallization leads to a predominant $\alpha$-PA6 crystalline phase, i.e., as in the initial sample at 30ºC (Fig. 6 Curve 4). On the contrary, the PA6-CL composite [Fig. 6(b)] displays a well-expressed initial $\gamma$-form at 30ºC with strong
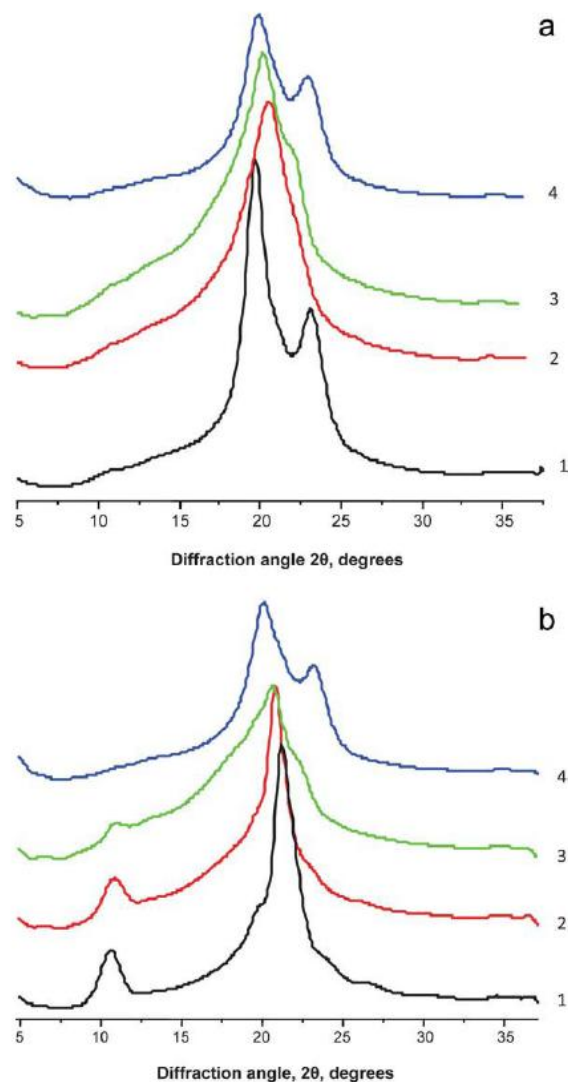


Figure 6 Temperature dependence of the WAXS reflections in two nanocomposites with 5 wt % of clay: a, Nanomer; b, Cloisite 15A. The numbers indicate the temperature at which the pattern was taken: 1, 30°C; 2, 160°C; 3, 200°C; 4, 30°C after melting at 260°C. [Color figure can be viewed in the online issue, which is available at wileyonlinelibrary.com.]

$\gamma$(020) reflection at 11º (Curve 1). Increasing the temperature to 160 and 200ºC results in a $\gamma$- to $\alpha$-form transition (Curves 2,3). After melting at 260ºC and Recrystallization a crystalline structure is achieved being very similar to that

TABLE V
**Long Spacing Data Obtained from the Fittings of the WAXS Patterns of PA6/MMT Nanocomposites**

| Sample | $d_{\alpha(200)}$ Å | $d_{\alpha(002/202)}$ Å | $d_{\gamma(001)}$ Å | $d_{\gamma(200)}$ Å | $d_{\gamma(020)}$ Å | Opal CT, Å (2θ position) |
|---|---|---|---|---|---|---|
| PA6 | 4.47 | 3.75 | 4.37 | 4.09 | – | – |
| 2.5% MMT | 4.38 | 3.76 | 4.14 | 4.06 | – | 3.97 (21.78) |
| 5.0% MMT | 4.38 | 3.73 | 4.11 | – | 8.21 | 3.95 (21.87) |
| 7.5% MMT | 4.39 | 3.88 | 4.17 | 4.09 | 8.18 | 3.97 (21.78) |
| 5.0% CL | 4.33 | 3.72 | 4.08 | – | 8.13 | 3.92 (22.01) |
| MB20NM | 4.34 | 3.86 | 4.08 | 4.06 | 7.98 | 3.95 (21.91) |
| MB10CL | 4.38 | 3.68 | 4.11 | – | 8.17 | 3.94 (21.93) |

of the NM-filled sample. The data in Table V show that the d-spacings of the PA6 crystalline peaks are independent of the amount and type of the MMT. The same is valid for the stronger MMT peak of the Opal CT.

On the basis of the WAXS data it may be concluded that admixing o-MMT to PA6 causes structural changes in both components. The changes in the MMT are related to the expansion of the galleries height and its eventual delamination. This is dependent on chemical treatment of the MMT source and on the way it has been introduced into the polymer, i.e., by in situ polymerization (as supposed in the case of the NM masterbacth) or simple melt-mixing, as in the case of the MB10CL. At the same time, the nanoclay type and amount cause changes in the crystallinity index of the PA6 matrix, as well in its polymorph content at various temperatures.

The good agreement between the DSC and WAXS data about the polymorph content should be noted. At the same time, the DSC crystallinity indices are always lower than those based on WAXS, although the general trend of crystallinity decrease with the increase of the filler was the same. Most probably, the X-ray method ''sees'' as ordered some domains that, upon heating, do not undergo typical melting, i.e., there is no contribution to the $\Delta H_m$. This is the concept of the so-called ''rigid amorphous phase'' introduced by Suzuki et al.[40] It should be noted that the difference between the WAXS and DSC crystallinity (Tables III and IV) grows as the MMT content increases suggesting an increase of the rigid amorphous phase in this direction.

## Structural studies by SAXS

Figure 7(a–c) displays some results of the SAXS studies on samples containing 1–20% Nanomer (Curves 2–5) compared with the PA6 matrix (Curves 1). As seen from the raw curve of PA6 in Figure 7(a), it has a clear maximum with zero intensity at diffraction vector values close to zero, typical of periodically arranged crystalline lamellae separated by amorphous phases. The appearance of such peaks is caused by the density difference between the crystalline and amorphous layers being relatively homogeneous in terms of their thickness.[41] Introducing even 1% of nanoclay into the PA6 matrix [Fig. 7(a) curve 2] results in nonzero scattered intensity at s=0, this effect being more pronounced at higher clay loads (Curves 3–5). Such curves are typical of systems where particulate phase is dispersed in a matrix,[42] i.e., as in the case of PA6-MMT nanocomposites.
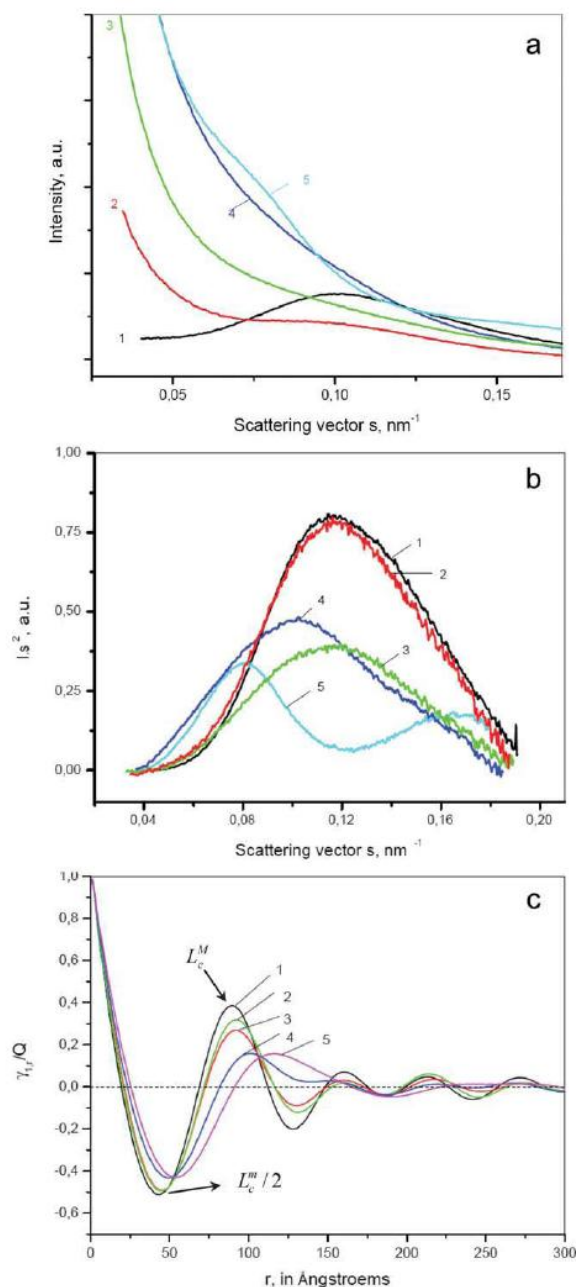


**Figure 7** SAXS data for PA6 nanocomposites containing vairous amounts of Nanomer obtained at 30°: a, raw patterns; b, Lorentz-corrected and normalized patterns; c, correlation functions calculated for the patterns in Figure 7(b). The numbers indicate the Nanomer concentration: 1, neat PA6 matrix; 2, 1%; 3, 2.5%; 4, 5.0%; 5, 20% (MB20NM). [Color figure can be viewed in the online issue, which is available at wileyonlinelibrary.com.]

**TABLE VI**
**Long Spacing Data Obtained from the Fittings of the WAXS Patterns of PA6/MMT Nanocomposites**

| Sample composition and WAXS crystallinity[a] | Structural parameters (SAXS) | |
| --- | --- | --- |
| PA6 no MMT<br>$CI_{WAXS} = 0.45$ | $L_B = 90$ Å<br>Lcm = 88 Å<br>LcM = 91 Å | $l_c = 60$ Å<br>$l_a = 31$ Å<br>$x_{cl} = 0.664$ |
| PA6 1% MMT<br>$CI_{WAXS} = 0.43$ | $L_B = 93$ Å<br>Lcm = 92 Å<br>LcM = 93 Å | $l_c = 61$ Å<br>$l_a = 32$ Å<br>$x_{cl} = 0.653$ |
| PA6 2.5% MMT<br>$CI_{WAXS} = 0.40$ | $L_B = 104$ Å<br>Lcm = 96 Å<br>LcM = 97 Å | $l_c = 64$ Å<br>$l_a = 33$ Å<br>$x_{cl} = 0.656$ |
| PA6 5.0 % MMT<br>$CI_{WAXS} = 0.38$ | $L_B = 120$ Å<br>Lcm = 102 Å<br>LcM = 102 Å | $l_c = 64$ Å<br>$l_a = 38$ Å<br>$x_{cl} = 0.629$ |
| PA6 20% MMT<br>$CI_{WAXS} = 0.34$ | $L_B = 132$ Å<br>Lcm = 110 Å<br>LcM = 117 Å | $l_c = 78$ Å<br>$l_a = 38$ Å<br>$x_{cl} = 0.667$ |

[a] As determined from WAXS in Table IV.
$CI_{WAXS}$, Crystallinity index by WAXS, for designation of the various types of long spacings see the text.

Figure 7(a) shows also that increasing the NM content from 1 to 5% results in an apparent diminution of the maximum related to the lamellar structure of the matrix. Interestingly, at 20% NM load (Curve 5) such maximum reappears at higher s values. To explain the shape of Curves 2–5 in Figure 7(a), one should bear in mind that the PA6-MMT nanostructure is supposed to combine lamellar-type periodicities (i.e., reciprocal lattice caused by the inherent heterogeneity of the semicrystalline PA6 matrix) and dispersed particulate phase from the MMT. Apparently, with the increase of the MMT content, the difference between the electronic densities of the amorphous and crystalline layers of the PA6 lamellar stacks is reduced resulting in lower intensities of the scattering peak. The reappearance of periodicity in Curve 5 may be related to the fact that the amorphous domains where MMT is probably accumulating became denser than that of the crystalline PA6 lamellae.

Figure 7(b) displays the Lorentz-corrected SAXS curves of the PA6 and its nanocomposites with NM. This treatment eliminates the characteristics of the particle scattering in the raw SAXS curves and can be used only wherever presence of reciprocal lattice type of structure is evidenced by a maximum in the raw SAXS curves. The composite with 1% and 2.5% of NM load (Curves 2,3) and the neat PA6 (Curve 1) produce very similar corrected SAXS profiles whose Bragg peak maxima LB nearly coincide, being in the range of 90–93 Å. The $L_B$ of the 5% NM composite display an upward shift to ca. 99 Å (Curve 4), while the masterbacth MB20NM (Curve 5) has two Bragg maxima at 124 and ca. 60 Å .

Cser[43] suggested that Lorentz-corrected SAXS data in semicrystalline polymers should be treated with caution due to a possible overlapping of the scattering of periodic lamellar structures and that of fractals and particles present in the system. In such systems, reportedly, the Lorentz correction may result in wrong positions of the Bragg peaks of the lamellar system or even in appearance of non- existing periodicity peaks. This warning may be valid in MMT nanocomposites where particle scattering is clearly observed [Fig. 7(a), 2-5]. That is why the linear correlation functions, CF, for the samples in Figure 7 were calculated and analyzed with the SASDAP software. [44] The respective curves are presented in Figure 7(c), and the structural data derived from them, in Table VI.

The linear CF was used by us previously for structural characterization of neat, isotropic PA6 samples.[38] First, the Bragg long spacing $L_B$ is determined as $1/s_{max}$ after subtraction of the liquid scattering contribution from the raw SAXS curves. Then, two additional estimates for the long spacing - from the position of the first maximum of CF (denoted as $L^M_c$) and from twice the position of the first minimum of CF ($L^m_c$)) are computed [Fig. 7(c), Table VI]. To calculate the values of the average thickness of the amorphous layer, ($l_a$) and the average lamellar thickness, ($l_c$) on the basis of CF, the following equation was used[45]:

$$\frac{B}{L_c^M} = x_{cl}(1 - x_{cl}) \quad (1)$$

where B is the position of the first intercept of CF with the r-axis and $x_{cl}$ being the crystalline fraction within the lamellar stack. The above quadratic equation has two solutions $x_1$ and $x_2$, whereby $x_1 + x_2. = 1$. For the samples in Table VI $x_1$ varies between 0.67 and 0.69 and $1-x_1$ - between 0.33 and 0.37, with the overall crystallinity fraction CI as determined by WAXS being between 0.34 and 0.45. Since the linear crystallinity within the stack is supposed to be higher than the overall CI, $x_1$ was assigned to $x_{cl}$ and ($1 - x_{cl}$) - to the amorphous fraction within the stack. Then, the $l_c$ and la were determined as[45]:

$$l_c = x_{cl}L_c^M \quad \text{and} \quad l_a = (1 - x_{cl})L_c^M \quad (2)$$

Analyzing the SAXS data from the CF analysis in Table VI, it can be concluded that increasing the load of Nanomer clay does not change $x_{cl}$ significantly, i.e., the crystallinity within the PA6 lamellar stacks is almost constant. At the same
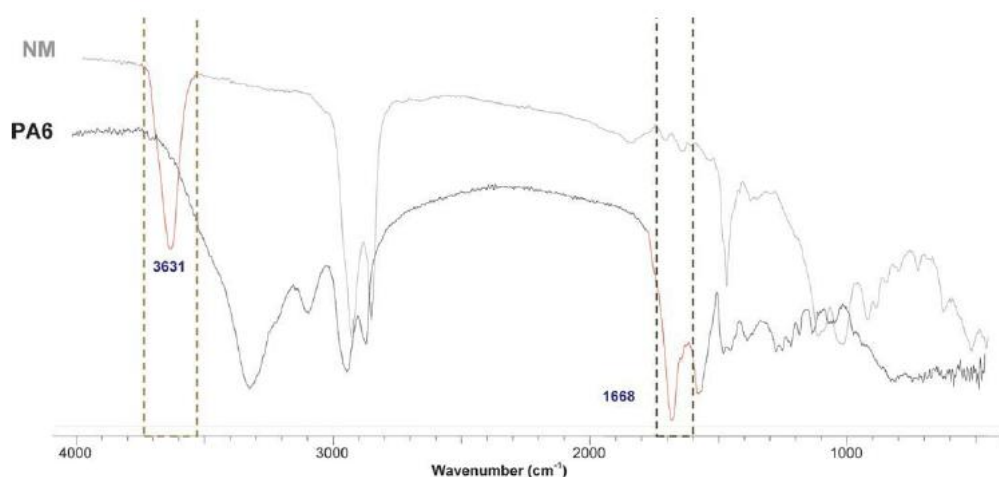
**Figure 8** FT-IR spectra in diffuse reflectance mode of Nanomer $o$-MMT (NM) and of the matrix polyamide 6 material (PA6). The rectangles show the wavelength areas used for the calibration of the FT-IR images in Figure 9: 3550–3700 cm$^{-1}$ for NM and 1600–1750 cm$^{-1}$ for PA6. [Color figure can be viewed in the online issue, which is available at wileyonlinelibrary.com.]

time, the periodicities become larger due to the growth of both $l_c$ and $l_a$. Since these effects are accompanied by a decrease of the overall crystallinity CI, it may be concluded that adding of more clay creates larger disordered areas ("liquid pockets") between the lamellar stacks of PA6 matrix. The $L^M_c$ value of the MB20NM sample as determined by the CF analysis is very close to the first maximum in the Lorentz corrected curve. Additional research is needed to establish whether or not the second maximum of this curve is an artifact or is related with a possible dual lamellar stack distribution caused by the increased clay load.

**FT-IR microscopy**

Even well-dispersed inorganic nanofillers naturally aggregate to form clusters whose size may extend above 1 lm. These aggregates are sometimes difficult to discover by electron microscopy techniques due to the small sample areas being investigated. However, scattering techniques that produce structural information integrated over larger areas show that aggregates in the micron length scale are present in all kind of nanocomposites regardless of the form of the primary nanoparticle—sphere, rod or sheet-like structures.46 The aggregates significantly limit the improvement of the mechanical properties of the nanocomposites especially if relatively hard matrices (as PA6 in the present case) are used.[47]

That is why as a concluding part of this study an attempt was made to evaluate the micron-scale homogeneity of the PA6-MMT nanocomposites by means of FT-IR microscopy.

Figure 8 shows the FT-IR spectrum of the organically modified Nanomer and of the neat PA6 matrix. The band at 3631 cm_1 in the NM sample is related to the stretching vibrations of nonassociated OH groups, chemically attach-ed to an Al atom of the MMT interlayers after the treatment MMT layer.[48] The absence of a broad band centered at 3400 cm$^{-1}$ shows that no water is contained in the MMT interlayers after the treatment. The peak at 1668 cm$^{-1}$ in the PA6 spectrum is related to the Amid-I band of the CO-NH group and is not present in the NM, just like the OH-peak does not exist in the PA6. Hence, these two peaks were used to produce the gray scale maps of the FT-IR microscopic images with a resolution of ca. 6.0 µm: white for 100% MMT, dark gray for 100% PA6.

Figure 9 shows the images for various nanocomposites and of the neat PA6 matrix over an area of ca. 500 x 400 µm. As expected, the neat PA6 is homogeneous in the length scale selected. The sample with 1% NM contains domains richer of MMT (the light gray spherical spots with diameters of 10–12 µm). These are embedded in a matrix that also contains some dispersed MMT below the resolution of the equipment, since the background is lighter than that of the pure PA6. Interestingly, the sample with 2.5% NM seems to be more homogeneous than the one with 1% NM, containing less in number but slightly larger MMT agglomerates, the background being also lighter than in the PA6 control. As the clay content grows to 5 and 7.5% NM, the background becomes slightly darker indicating that the PA6 matrix contains less MMT. At the same time, the FT-IR microscopy method does not discover big differences in the agglomerations of the nano-composites with 5% NM, 5% CL, and 7.5% NM. From the two masterbatches MB10CL and MB20NM, however, the second one is much more heterogeneous showing large continuous areas with increased clay concentration.

The small dark-gray spots indicating PA6 richer domains appear only in this sample and may be due to the fact that it was produced by in situ polymerization and not by mixing of MMT to a PA6 polymer.
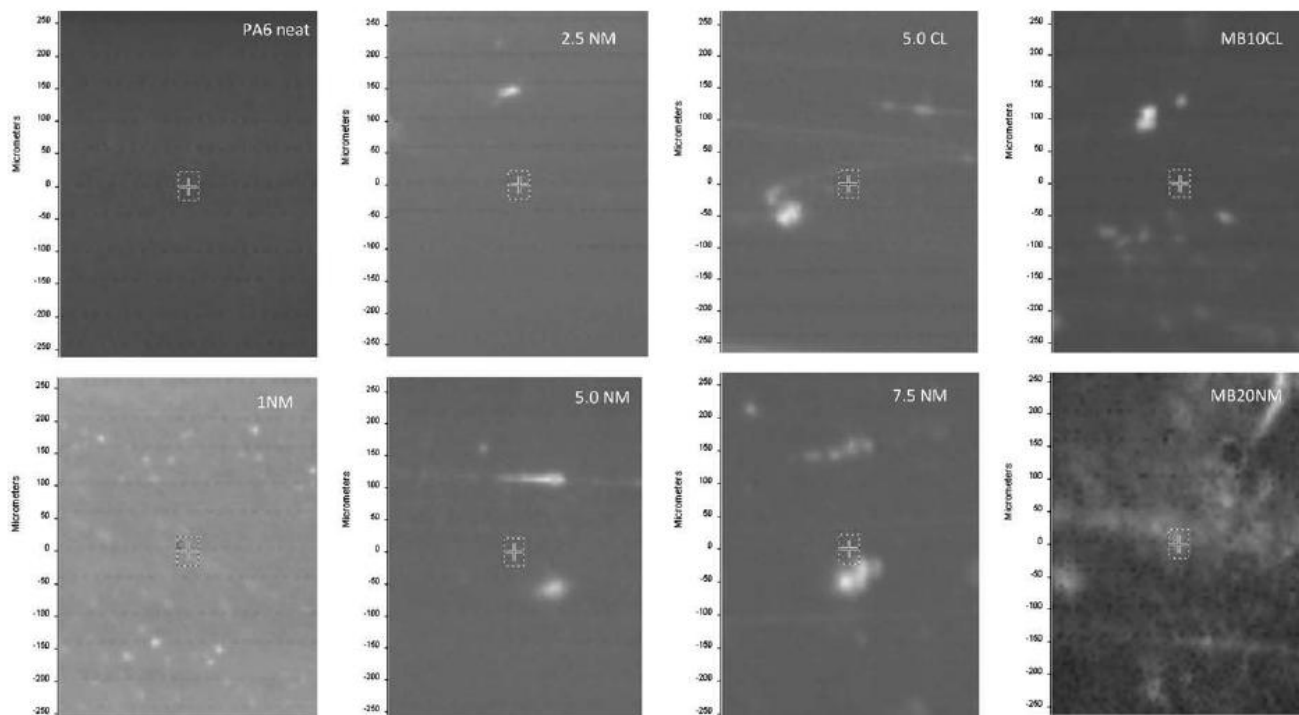
**Figure 9** FT-IR imaging in PA6/MMT nanocomposites. The mapping is based on the peaks in Figure 8. The white color corresponds to the MMT and the dark gray—to the PA6 domains. [Color figure can be viewed in the online issue, which is available at wileyonlinelibrary.com.]

## CONCLUSIONS

Based on the combined mechanical, thermal, X-ray, and FT-IR microscopy analyses, the following conclusions can be drawn on the structure-properties relationship in the PA6/MMT nanocomposites in this study:

1. The tensile behavior (Young modulus and tensile strength) of the nanocomposites depend in a different way on the concentration and type of the MMT source: while the modulus grows proportionally to the clay content, the tensile strength passes through a maximum at ca. 2.5% MMT. Comparing the properties of samples 5% NM and 5% CL, it seems that that Nanomer-modified PA6 is stronger and stiffer. A possible structural explanation can be the higher aspect ratio of the Nanomer monolayers—up to 400, while in Cloisite 15A it only reaches 100.

2. The presence of clay aggregation at micron length scale results in higher modulus, while the tensile strength is better in homogeneous samples, as revealed by FT-IR microscopy.

3. The gallery heights in Nanomer and Cloisite clays after organophilization expand from 10 to 12 Å to 20 and 29 Å, respectively. The introduction of PA6 results in a further enlargement to 45–48 Å, suggesting an average tactoid arrangement of the MMT layers within the area of X-ray irradiation of ca. 1.5 mm$^2$. This finding is in agreement with the FT-IR microscopy results.

4. Increasing the amount of MMT results in a lower crystallinity of the PA6-matrix and significantly increases the amount of γ-PA6 polymorph, this trend being better expressed with Cloisite clay.

5. The MMT clay enhances the formation in the PA6 matrix of larger periodicities (lamellar stacks) with long spacings growing from 90 to ca. 120 Å due to expansion of both crystalline and amorphous layers.

### References

1. Alexandre, M.; Dubois, P. Mater Sci Eng 2000, 28, 1.
2. Fornes, T. D.; Yoon, P. J.; Keskulla, H.; Paul, D. R. Polymer 2002, 43, 5915.
3. Tjong, S. C.; Bao, S. P. J Polym Sci: Part B: Polym Phys 2004,42, 2878.
4. Fornes, T. D.; Hunter, D. L.; Paul, D. R. Polymer 2004, 45, 2321.
5. Gilman, J. W. Appl Clay Sci 1999, 15, 31.
6. Giannelis, E. P. Appl Organomet Chem 1998, 12, 675.
7. Kojima, Y.; Usuki, A.; Kawasumi, M.; Okada, A.; Kurauchi, T.; Kamigaito, O. J Polym Sci Part A: Polym Chem 1993, 31, 983.
8. Kojima, Y.; Usuki, A.; Kawasumi, M.; Okada, A.; Kurauchi, T.; Kamigaito, O. J Polym Sci Part A: Polym Chem 1993, 31, 1755.
9. Gilman, J. W.; Jackson, C. L.; Morgan, A. B.; Harris, R., Jr.; Manias, E.; Giannelis, E. P.; Wuthenow, M.; Hilton, D.; Philips, S. H. Chem Mater 2000, 12, 1866.
10. Gilman, J. W.; Kashiwagi, T.; Lichtenhan, J. D. SAMPE J 1999, 33, 40.

11. Yano, K.; Usuki, A.; Okada, A.; Kurauchi, T.; Kamigaito, O. J Polym Sci Part A: Polym Chem 1993, 31, 2493.

12. Yano, K.; Usuki, A.; Okada, A. J Polym Sci Part A: Polym Chem 1997, 35, 2289.

13. Avella, M.; Bondioli, F.; Cannillo, V.; Di Pace, E.; Errico, M. E.; Ferrari, A. M.; Focher, B.; Malinconico, M. Compos Sci Technol 2006, 66, 886.

14. Osman, M. A.; Ploetze, M.; Skrabal, P. J; Phys Chem 2004,B108, 2580.

15. Tjong, S. C. Mater Sci Eng 2006, R53, 73.

16. Ray, S. S.; Okamoto, M. Prog Polym Sci 2003, 28, 1539.

17. Shelley, J. S.; Mather, P. T.; DeVries, K. L. Polymer 2001, 42, 5849.

18. Xie, S.; Zhang, S.; Liu, H.; Chen, G.; Wang, F.; Yang, M. Polymer 2005, 46, 5417.

19. Yang, K.; Ozisik, R. Polymer 2006, 47, 2849.

20. Kamigaito, O.; Fukushima, Y.; Doi, H. US Patent 4,472,538, 1984.

21. Usuki, A.; Kojima, Y.; Kawasumi, M.; Okada, A.;Kurauchi, T.;Kamigaito, O. ACS Polymer 1990, 31, 651.

22. Ibanes, C.; de Boissieu, M.; David, L.; Seguela, R. Polymer 2006, 47, 5071.

23. Ito, M.; Takahashi, A.; Araki, N.; Kanamoto, T. Polymer 2001, 42, 241.

24. Lincoln, D. M.; Vaia, R. A.; Wang, Z.-G.; Hsiao, B. S. Polymer 2001, 42, 1621.

25. Lincoln, D. M.; Vaia, R. A.; Wang, Z.-G.; Hsiao, B. S.; Krishnamoorti,R. Polymer 2001, 42, 9975.

26. Lincoln, D. M.; Vaia, R. A. Macromolecules 2004, 37, 4554.

27. Varlot, K.; Reynaud, E.; Kloppfer, M. H.; Vigier, G.; Varlet, J.J Polym Sci Part B: Polym Phys 2001, 39, 1360.

28. Ibanes, C.; David, L.; de Biossieu, M.; Seguela, R.; Epicier, T.; Robert, G. J Polym Sci: Part B: Polym Phys 2004, 42, 3876.

29. Hasegawa, N.; Okamoto, H.; Kato, M.; Usuki, A.; Sato, N. Polymer 2003, 44, 2933.

30. Fedullo, N.; Sclavons, M.; Bailly, C.; Lefebre, J. M.; Devaux, J. Macromol Symp 2006, 233, 235.

31. Liu, X.; Wu, Q. Eur Polym J 2002, 38, 1383.

32. Loo, L. S.; Gleason, K. K. Polymer 2004, 45, 5933.

33. Tsai, Y.; Wu, J.-H.; Leu, M.-T. Polym Adv Technol 2010 (DOI: 10.1002/pat. 1764).

33. Dencheva, N.; Oliveira, M. J.; Carneiro, O. S.; Pouzada, A. S.; Denchev, Z. J Appl Polym Sci 2010, 115, 2918.

34.POLAR, version 2.7.3; CopyrightVC 1997–2008 by Stonybrook Technology and Applied research, Inc, USA.

35. Usuki, A.; Hasegawa, N.; Kadoura, H.; Okamoto, T. Nanoletters 2001, 1, 271.

36. Koh, S.-M. New Understanding of Clay Minerals, CASM Asia-Pacific Meeting, Bandung, Indonesia, November 2006.

37. Guthrie, G. D.; Bish, D. L.; Reynolds, R. C. Am Mineralogist 1995, 80, 869.

38. Dencheva, N.; Nunes, T.; Oliveira, M. J.; Denchev, Z. Polymer 2005, 46, 887.

39. Fornes, T. D.; Paul, D. R. Polymer 2003, 44, 3945.

40. Suzuki, H.; Grebowicz, J.; Wunderlich, B. Makromol Chem 1984, 186, 1109.

41. Bassett, D. C. Principles of Polymer Morphology; Cambridge University Press: Cambridge, 1981.

42. Glatter, O.; Kratky, O. Small Angle X-ray Scattering; Academic Press: London, 1982.

43. Cser, F. J Appl Polym Sci 2001, 80, 2300.

44. SASDAP, Copyright (c) 1995 by R. Verma, A. Biswas, and B. Hsiao, DuPont Experimental Station, Wilmington, DE, USA.

45. Santa Cruz, C.; Stribeck, N.; Zachmann, H. G.; Balta´-Calleja, F.J Macromolecules 1991, 24, 5980.

46. Brown, J. M.; Anderson, D. P.; Justice, R. S.; Lafdi, K.; Belfor,M.; Strong, K. L.; Schaefer, D. W. Polymer 2005, 46, 10854.

47. Schaefer, D. W.; Justice, R. S. Macromolecules 2007, 40, 8501.

48. Seiffarth, T.; Kaps, C. Clays Clay Minerals 2009, 57, 40.